Geophys. J. Int. (2006) **167,** 77–88 doi: 10.1111/j.1365-246X.2006.02889.x

Numerical modelling of generation, propagation and run-up of tsunamis caused by oceanic impacts: model strategy and technical solutions

Robert Weiss,[1,3] Kai Wünnemann[2] and Heinrich Bahlburg[3]

[1]*Joint Institute for the Study of the Atmosphere and Ocean, University of Washington—National Center for Tsunami Research, Pacific Marine Environmental Laboratory,* 7600 *Sand Point Way NE, Seattle, WA* 98115, *USA. E-mail: weiszr@u.washington.edu*
[2]*Institut für Mineralogie, Museum für Naturkunde, Humboldt-Universität zu Berlin, Invalidenstraße* 43, 10115 *Berlin, Germany*
[3]*Geologisch-Paläontologisches Institut und Museum, Westfälische Wilhelms Universität Münster, Corrensstraße* 24, 48149 *Münster, Germany*

Accepted 2005 December 16. Received 2005 December 7; in original form 2005 January 23

SUMMARY

Hypervelocity impacts of asteroids in marine environments produce tsunami waves independent of the water depth and the diameter of the projectile. However, the characteristics of the induced waves are affected by these parameters. We present a model, consisting of the well-known SALE impact model and a non-linear wave propagation model, to study the generation and subsequent spread out of the initial wave pattern caused by the strike of an asteroid or comet in the ocean. The numerical simulation of oceanic impacts requires some changes and extensions to the original SALE code. Especially, the handling of different materials (water and solid rocks) is crucial as they are involved in the cratering process. For the simulation of the propagation of tsunami waves that are generated by the impact process we use a newly developed wave propagation model, which is based on the non-linear shallow water theory with boundary conditions derived from the impact model. The run-up of the tsunami wave on the coastline is implemented as a special case of reflection and is realized by the well-established MOST code. Besides the model description we exemplify the capability of our modelling scheme by the simulation of the strike of an asteroid 800 m in diameter on a 5000-m-deep ocean at 10.2 km s^{-1}, the subsequent propagation of the induced tsunami waves over an artificial bathymetry and the run-up of the wave on the coast.

Key words: hydrocode modelling, impact cratering, long wave run-up, Oceanic impacts, tsunami wave propagation.

1 INTRODUCTION

The probability of an asteroid or comet impacting on water is much higher than for continental sites because two-thirds of the Earth's surface is covered by oceans. Depending on the size of the projectile (asteroid or comet), impact events are directly linked to environmental perturbations on local, regional and global scales. Oceanic impacts have distinct consequences in comparison to the strike of a bolide on land due to the water masses involved in the cratering process. The most striking difference is the generation of tsunami waves (Crawford & Mader 1998; Paine 1999; Ward & Asphaug 2000; Shuvalov *et al.* 2002).

Tsunami may cause extensive damage even several thousands of kilometres away from the point of impact. Therefore, it is important to investigate the destructive force of these waves as a function of distance from impact, and the local bathymetry. Apparently the ratio of the water depth at the impact site to the size of the projectile is an important parameter assessing the magnitude of the generated waves (Crawford & Mader 1998; Shuvalov *et al.* 2002).

If the impact energy of the bolide striking the Earth's surface is assumed to be constant, the water depth is the controlling parameter to determine the characteristics and quantity of the induced waves (Weiß *et al.* 2003). The ratio γ between the water depth H and the diameter of the projectile d ($\gamma = H/d$) can be used to evaluate the influence of the water depth on the cratering process, if the impact velocity and density of the projectile are kept constant (Artemieva & Shuvalov 2002).

If $\gamma > 10$, the kinetic energy of the bolide is not sufficient to penetrate the water column. No crater structure is formed in the oceanic crust and only tsunami waves are generated. If γ is between 10 and 1, the water column has a strong influence on the crater formation in the ocean bottom. The morphology of these craters differs in several respects from those on continents (Gault & Sonett 1982; Ormö *et al.* 2002; Shuvalov *et al.* 2002). If $\gamma < 0.1$, the presence of water can be neglected regarding the crater formation process, and the resulting morphology of the crater structures is similar to impact craters on continents (Artemieva & Shuvalov 2002). Nevertheless, tsunami waves are generated although the water depth is very small.

© 2006 The Authors
Journal compilation © 2006 RAS

There are two different wave generation mechanisms accompanying the strike of an asteroid in an ocean that trigger tsunami waves: (i) The excavation of a crater in the ocean bottom gives rise to the ejection of material out of the crater and the formation of a crater rim. Driven by gravity, the crater rim eventually collapses and flaps onto the water surface causing the generation of the first type of tsunami waves referred to as 'rim wave'. (ii) The collapse of the transient cavity in the water column, formed by the penetration of the projectile, results in the generation of a second kind of tsunami wave referred to as 'collapse wave'.

The present understanding of tsunami in general induced by other sources like, for example, tectonic deformations due to earthquakes or landslides are discussed in Synolakis (1986, 1987), Synolakis *et al.* (2001) and Tadepalli & Synolakis (1994). For oceanic impacts, a variety of numerical models have been proposed to quantify the generation, propagation and inundation (e.g. Mader 1998a,b; Crawford & Mader 1998; Paine 1999; Ward & Asphang 2000; Matsui *et al.* 2002). Only one of them, for example, Crawford & Mader (1998) uses a combination of impact and tsunami modelling. They utilized the well-known CTH code (McGlaun & Thomspon 1990) to compute the impact process and the maximum excavation in the water. Then the ZUNI model, proposed by Amsden (1973) and Mader (1988), is used to simulate the collapse of the cavity and propagation of tsunamis. Following a similar strategy, we present a combination of the SALE code (Amsden *et al.* 1980; Wünnemann & Lange 2002; Wünnemann & Ivanov 2003; Wünnemann *et al.* 2005) and a newly developed non-linear tsunami wave propagation model to simulate impact-related tsunamis. Crawford & Mader (1998) discuss only deep-water impacts. In principle our model strategy is applicable to impact scenarios with any kind of water depths. For instance the impact model was used to simulate shallow water impact events like the Chesapeake Bay impact (Collins & Wünnemann 2005) where the water depth was very small, only a few hundred metres, in comparison to the size of the impactor (several kilometres). In this study we present an example where the diameter of the projectile was only a fraction of the water depth as it was the case at the Eltanin impact in the south Polar sea (e.g. Gersonde *et al.* 1997; Wünnemann & Lange 2002).

We first elucidate the principal ideas of the SALE hydrocode that consider the impact process and the generation of the initial wave pattern. Then, the structure of the 2-D non-linear tsunami wave propagation and run-up model are described. The third section presents results of the impact of a 800 m diameter asteroid striking a 5000-m-deep ocean at 10.2 km s^{-1}.

2 GENERATION OF IMPACT-RELATED TSUNAMIS

To investigate the generation of tsunami waves by oceanic impact events we utilize a numerical model to simulate the cratering process, beginning with the first contact of the asteroid and the water surface. A number of models have been proposed to compute the high velocity strike of an asteroid on both solid and oceanic targets (e.g. Roddy *et al.* 1987; O'Keefe & Ahrens 1999; Ivanov & Artemieva 2002, Shuvalov *et al.* 2002; Wünnemann & Lange 2001; Wünnemann *et al.* 2005). All hydrocodes, used to model impact cratering, (e.g. CTH, McGlaun *et al.* 1990, and SOVA, Shuvalov 1999) assume a continuum of the entire spatial area involved in the cratering process. This assumption allows describing the behaviour of material by a set of differential equations based on the conservation of mass, momentum and energy. In addition, an equation of state (EOS) characterizing the thermodynamic state of the material at high pressure and temperature as well as the elasto-plastic response of rocks to strong deformations in terms of failure mechanisms (constitutive equations; CE) are required. A general overview of hydrocode modelling is given in Anderson (1987) or Knowles & Brode (1977), respectively.

The simulation of an oceanic impact and the generation of tsunami waves impose special demands on the model in terms of different material layering of the target (basement rocks, sediments, water, and empty space or void) and due to the large deformations taking place. We use the iSALE hydrocode (e.g. Wünnenmann *et al.* 2006), which was used in several impact studies before (Goldin *et al.* 2005; Wünnemann *et al.* 2005; Collins & Wünnemann 2005). The code is based on the original version by Amsden *et al.* (1980) and is basically very similar to the well-known version SALEB by Ivanov *et al.* (1997). The major difference consists in the possibility to involve up to three different material types in the model, whereas SALEB can handle only two. We present here a more detailed description of how to deal with different materials in Eulerian mode hydrocode calculations and how to track sharp material boundaries.

2.1 The Lagrangian/Eulerian kinematic model

As in most hydrocodes, the computational domain is discretized in a grid of cells with a specified size (*dx, dy*) to replace the spatial derivatives in the differential equations by simple (finite) difference equations. Two different kinematic models can be used: (i) The Eulerian and (ii) the Lagrangian description. An introduction to the different kinematic models is given by for example, Anderson (1987). The difference lies in principle in the way how mass, energy and momentum are transported through the grid. In the Lagrangian kinematic model, matter is associated with a cell. Material motions are calculated by the deformation of the cell, yielding a distortion of the entire grid. Large deformations can produce spurious results, if the deformations of the cells are severe. In contrast, the dynamic motions of mass, momentum and energy are realized in the Eulerian mod by computing the transport between adjacent cells.

The Eulerian description appears much more suitable for impact calculations, since we have to deal with very large deformations, fluid flow and phase transitions. However, the transport of mass across cell boundaries gives rise to artificial mixing of different kinds of matter along material boundaries, referred to as artificial numerical diffusion. For example, in the present study the model implies boundaries between water and solid rock or between matter (basement rock, sediment or water) and void (empty space or vacuum, an atmospheric pressure is not taken into account). The material transport from one cell to one of the adjacent cells, which potentially contains a different kind of matter, yields mixed cells with at least two different materials. Finally, sharp boundaries, for instance the free surface, become more diffuse the more time steps have been integrated. The free surface depicts the interface between matter- and vacuum-filled (void) grid cells in our model and is very important to determine the wave height, which is a crucial parameter regarding the objective of the present paper.

2.2 Internal material boundaries for the Eulerian kinematic model

To avoid material mixing and to preserve sharp material boundaries we introduce a procedure to the original code, to construct internal cell boundaries between different kinds of matter or between matter

and void (free surface) in cells containing a mixture of materials. By means of the volume fraction of each material in the actual cell and the adjacent ones the internal boundaries between void and matter or between rock and water, respectively, are calculated. This means, if all three or four kinds of material (basement/sedimentary rocks, water, void) are present at once in a cell, two or three internal boundaries have to be constructed. In consideration of the positions of the internal boundaries, the transport of mass between adjacent cells (advection) is carried out. These simple assumptions allow the advection of matter, while preserving clear boundaries along the free surface, and between water and rocks.

Fig. 1 shows a simple numerical simulation of a block impacting on a target using the three different solution schemes: Pure Lagrangian, pure Eulerian and the Eulerian mode containing the construction of internal cell boundaries along the free surface. For simplicity there is only one boundary between void and matter in this example; different kinds of matter (water, rock) are not involved. Although the Lagrangian model (Fig. 1a) shows a sharp free surface boundary the cell deformations become large and thus, the finite difference approximation is inaccurate. In the Eulerian model (Fig. 1b) the numerical solution is stable, but there is no sharp boundary between matter and void. As the last example (Fig. 1c) shows, introducing internal cell boundaries enables the computation of any deformation while conserving a well-defined free surface. Similar to the example of the free surface, material boundaries between solid rock and water or basement and sediment can be calculated.

2.3 Constitutive Equations (CE) and model setup

To compute the thermodynamic state of the material we use the Analytical Equation of State (ANEOS, Thompson & Lauson 1972) for water and granite. A more realistic assumption would be the usage of basalt instead of granite for the ocean crust. Unfortunately ANEOS is yet not capable to handle basaltic material. In general, the thermodynamic properties of the ocean crust material play only a minor role in crater formation and can be neglected for the simulation of the wave characteristic induced by the impact process. In our model we assume that water behaves purely hydrodynamically without any viscosity. In contrast rocks behave plastically (ductile) only beyond a

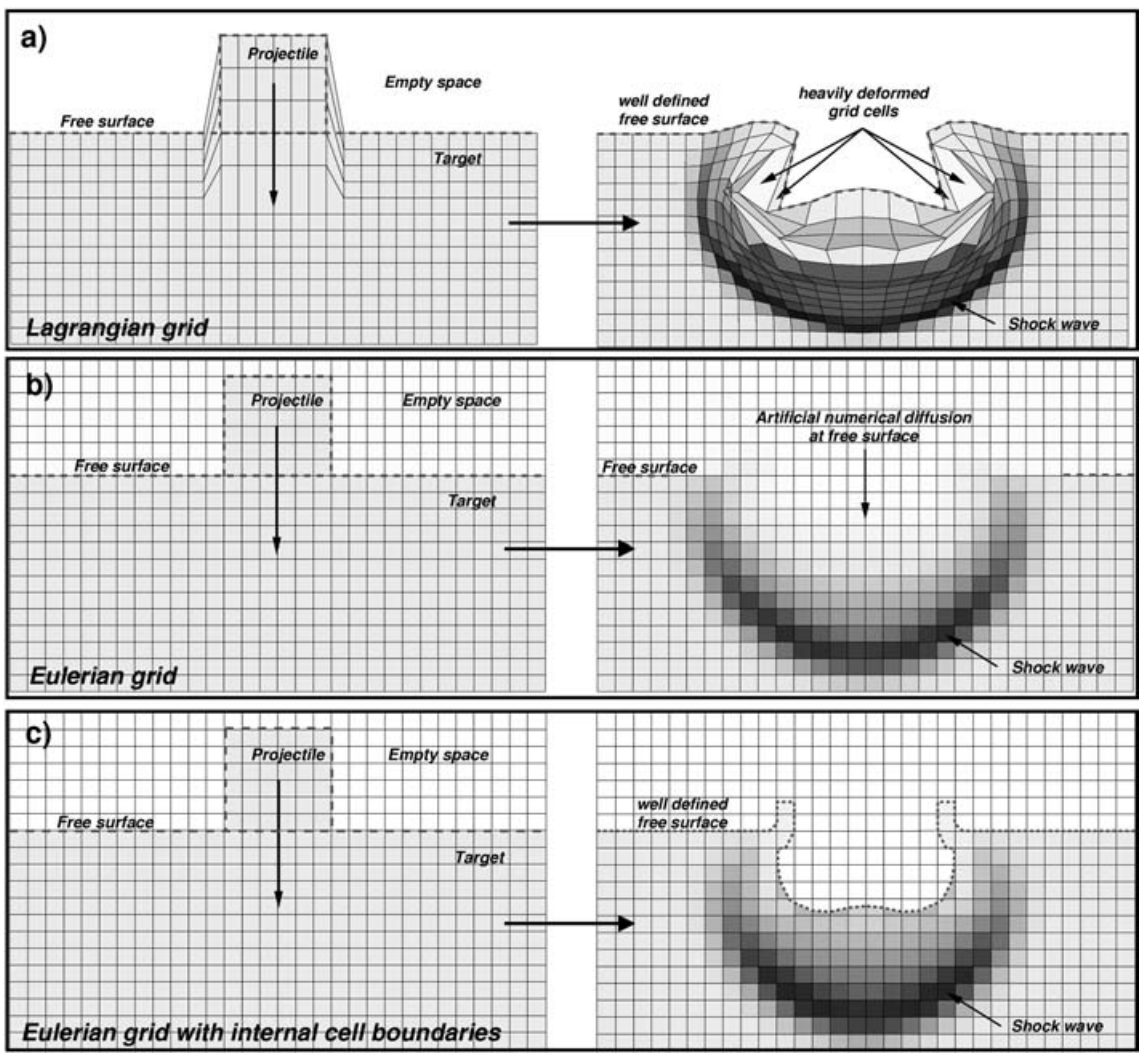

Figure 1. Comparison between the numerical models of the impact of a projectile on a target using different kinematic models. The Eulerian description results in an artificial numerical diffusion along the free-surface. In the Lagrangian description spurious results occur due to large deformations of numerical cells. The introduction of internal cell boundaries in the Eulerian solution scheme allows the computation of large deformations while preserving material boundaries.

© 2006 The Authors, *GJI*, **167,** 77–88
Journal compilation © 2006 RAS

certain yield point. Below the so-called plastic yield strength Y rocks respond elastically to the given stress. The elastic failure of rocks is calculated by the von Mises yield criterion, wherein strength Y is a function of pressure and temperature $Y = f(p, T)$. A detailed description of CE is given in Wünnemann & Ivanov (2003) and Collins *et al.* (2004).

All models in the present study are carried out on a computational grid of 700 × 450 cells in radial and vertical direction, respectively. The sketch in Fig. 2 illustrates the setup of the computational domain. We use a cylindrical grid geometry with the left boundary being the axial symmetry axis. The 2-D geometry constrains the model to vertical impacts only. We use 'free-slip' boundary condition in radial direction and at the top of the mesh and 'no-slip' condition at the bottom of the grid. To avoid any interfering reflections of waves, when they hit the boundary of the computational grid, we expand the outer 70 cells in each direction (r- and z-direction, see Fig. 2) by a factor of 1.05 (e.g. $dx_{n+1} = 1.05 \times dx_n$, where dx is the spatial increment). Thereby we can cover a much larger area with the computational domain so that the amplitude of the waves (for instance shock waves) generated by the impact process have decreased significantly before they are reflected at the grid boundaries and no interfering effects between reflected waves and the generated tsunami waves can occur. The spatial resolution is 50 m in the inner (high resolution) area in the vicinity of the point of impact and the maximum cell size at the boundary of the grid (in the expanded area) is maximal ~400 m. The total grid covers an area of approximately 43.7 × 33.8 km. The impactor has a diameter of 16 cells (800 m) and hits the surface at a velocity of 10.2 km s^{-1}. The water column is represented by a layer of 100 cells (5000 m). In previous test calculations we found that 10 cells per material layer is the lower resolution limit to assure a stable solution of the problem but at least 20 cells are generally aspired.

We do not consider an atmosphere in our models, and assume that cells containing neither water nor rock are empty. A set of snapshots of an oceanic impact at different points in time is shown in Fig. 3.

3 PROPAGATION MODEL WITH RUN-UP

The numerical simulation of the propagation and run-up of tsunami waves represents a central part of our modelling study. Therefore, we discuss our novel implementation of the wave propagation model here more in detail.

Classical approaches simulating the propagation of tsunami waves are the shallow water equations (SWE; Synolakis 1987) and the Bousinesq equations (BE; Peregrine 1967). SWE and BE are depth-integrated approaches regarding the velocity field (no velocity variations with depth). For example, SWE can be easily obtained by integrating the Euler equation with respect to depth. As demonstrated later, SWE can be also derived by neglecting the dispersive terms in the BE.

The starting point of our hydrodynamical model is the Boussinesq approach proposed by Perigrine (1967). Beji & Nadaoka (1996) expanded the BE with special regard to an improvement of the dispersive characteristics:

$$\nabla_t \vec{w} + \vec{w}(\nabla_h \cdot \vec{w}) + g\nabla_h \eta = \vec{D}$$
$$\text{with } \vec{D} = (1-\beta)\frac{h}{2}\nabla_h\left[\nabla_h \cdot \left(h\frac{\partial \vec{w}}{\partial t}\right)\right] - \beta\frac{h^2}{6}\nabla_h\left(\nabla_h \cdot \frac{\partial \vec{w}}{\partial t}\right)$$
$$+\beta\frac{gh}{2}\nabla_h\left[\nabla_h \cdot (h\nabla_h \eta)\right] - \beta\frac{gh^2}{6}\nabla_h[\nabla^2\eta], \quad (1)$$

where $\vec{w}$ represents the horizontal velocity field, h is the water depth, η denotes the surface elevation due to the wave and g is the

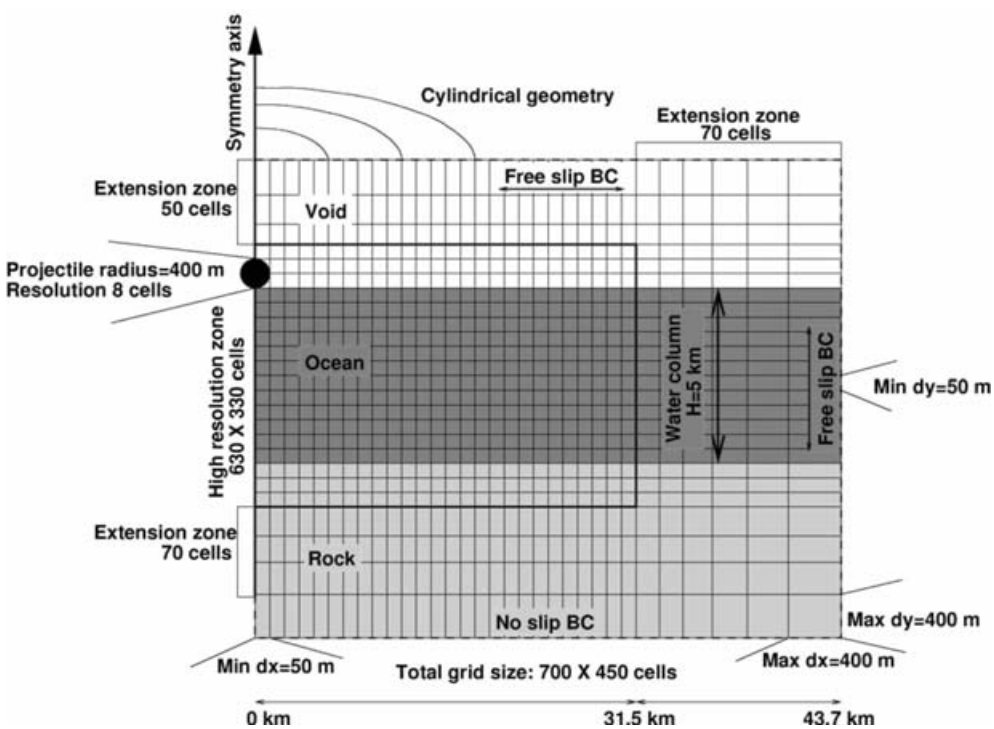

Figure 2. Set-up of the SALE-3MAT computational grid. Note the cylindrical geometry of the grid. For simplicity the sketch shows a reduced number of cells only. The outer 70 cells in r- and z-direction and the upper 50 cells are extended by a factor of 1.05 to rule out interfering wave reflections from the grid boundaries.

© 2006 The Authors, *GJI*, **167,** 77–88
Journal compilation © 2006 RAS

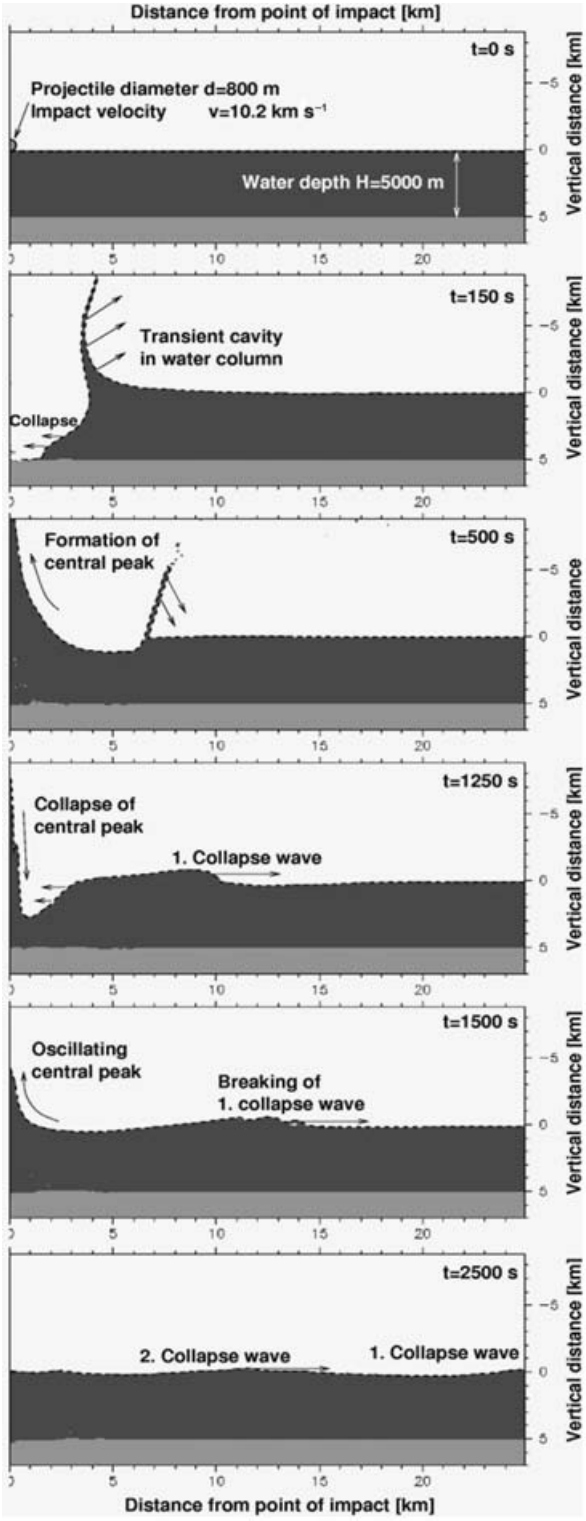

Figure 3. Snapshot series of the impact of an asteroid 800 m in diameter striking an 5000-m-deep water at 10.2 km s^{-1}. Different stages of crater formation and wave generation are illustrated: ($t = 0$ s) initial state, the projectile first touches the surface of the water; ($t = 150$ s) formation of the transient crater, which describes the approximate maximum extent of the cavity; ($t = 500$ s) the transient cavity has collapsed and a central peak has formed; ($t = 1250$ s) driven by gravity the central peak collapses and triggers the first wave; ($t = 1500$) oscillations of the central peak result in the generation of a series of subsequent waves; ($t = 2500$ s) final wave characteristic consisting of three different wave signals.

gravity. The parameter β controls the dispersive properties of eq. (1) and is commonly set to $\beta = 1/5$ (Beji & Nadaoka 1996). Eq. (1) gives reliable results for a maximum depth to wavelength ratio of $h/\lambda = 0.25$–0.5 (Perigrine 1967; Beji & Nadaoko 1996; Lynett & Liu 2002).

Eq. (1) separates non-dispersive elements on the left-hand side from dispersive elements on the right-hand side. The right-hand side of eq. 1 is now substituted by the parameter D which denotes the dispersive elements. If $D = 0$ the conditions for the SWE are satisfied. Both cases $D = 0$ and $D > 0$ (corresponding to the right-hand side of eq. 1), are utilized as a momentum equation of the hydrodynamic model. It is used to simulate the propagation of impact-induced tsunami waves. Complementing the approach the following equation of continuity is used:

$$\nabla_t \eta + [h + \eta](\nabla_h \cdot \vec{w}) + \vec{w} \cdot \nabla_h [h + \eta] = 0. \tag{2}$$

The finite difference scheme is utilized to implement eqs (1) and (2) in a computer model.

3.1 Basic numerical scheme and boundary conditions

Considering the complete set of equations in (1) results in a large number of terms. To keep the computational problem simple, we split the terms and omit all orthogonal and spatially mixed derivatives. The resulting equations read:

$$\begin{aligned} \frac{\partial u}{\partial t} + u\frac{\partial u}{\partial x} + v\frac{\partial u}{\partial y} + g\frac{\partial \eta}{\partial x} &= \vec{D}_u \\ \frac{\partial v}{\partial t} + u\frac{\partial v}{\partial x} + v\frac{\partial v}{\partial y} + g\frac{\partial \eta}{\partial y} &= \vec{D}_v, \end{aligned} \tag{3}$$

with

$$\begin{aligned} \vec{D}_u = {} & (1-\beta)h\left[\frac{h}{2}\frac{\partial^3 u}{\partial x^3} + \frac{\partial h}{\partial x}\frac{\partial^2 u}{\partial x \partial t} + \frac{1}{2}\frac{\partial u}{\partial x}\frac{\partial^2 h}{\partial x^2}\right] \\ & -\beta\frac{h^2}{3}\left[\frac{\partial^3 u}{\partial x^2 \partial t} + g\frac{\partial^3 \eta}{\partial x^3}\right] \\ & +\beta\frac{hg}{2}\left[h\frac{\partial^3 \eta}{\partial x^3} + 2\frac{\partial h}{\partial x}\frac{\partial^2 \eta}{\partial x^2} + \frac{\partial \eta}{\partial x}\frac{\partial^2 h}{\partial x^2}\right] \\ \vec{D}_v = {} & (1-\beta)h\left[\frac{h}{2}\frac{\partial^3 v}{\partial y^3} + \frac{\partial h}{\partial y}\frac{\partial^2 v}{\partial y \partial t} + \frac{1}{2}\frac{\partial v}{\partial y}\frac{\partial^2 h}{\partial y^2}\right] \\ & -\beta\frac{h^2}{3}\left[\frac{\partial^3 v}{\partial y^2 \partial t} + g\frac{\partial^3 \eta}{\partial y^3}\right] \\ & +\beta\frac{hg}{2}\left[h\frac{\partial^3 \eta}{\partial y^3} + 2\frac{\partial h}{\partial y}\frac{\partial^2 \eta}{\partial y^2} + \frac{\partial \eta}{\partial y}\frac{\partial^2 h}{\partial y^2}\right]. \end{aligned} \tag{4}$$

In both equations (eqs 3 and 4), u and v represent the orthogonal components of the horizontal velocity field $\vec{w}$. Eqs (3) and (4) are numerically solved on a 2-D Eulerian mesh, resulting in a classic '2+1' problem. As already outlined, this approach is depth-integrated and, therefore, no discretization along the vertical is required. The solution technique corresponds to a centred finite difference scheme, including the Lax method (Press *et al.* 1992). According to Perigrine (1967) it can be used for dispersive computations. For non-dispersive elements, numerical operators are defined as:

$$\begin{aligned} \delta^{(t)} f &= \frac{1}{\Delta t}(f(x, y, t+1) - f(x, y, t)), \\ \delta^{(x,t)} f &= \frac{1}{2\Delta x}(f(x+1, y, t) - f(x-1, y, t)) \end{aligned}$$

© 2006 The Authors, *GJI*, **167,** 77–88
Journal compilation © 2006 RAS

and

$$\delta_{LAX} f = \frac{1}{4}(f(x+1,y,t) + f(x-1,y,t) + f(x,y+1,t) + f(x,y-1,t))$$

With the help of these operators, eqs (2) and (3) can be written as:
Momentum equations:

$$\begin{aligned} \delta^{(t)}_{LAX}\mathbf{u} &= -\mathbf{u}\delta^{(x)}\mathbf{u} - v\delta^{(y)}\mathbf{u} - g\delta^{(x)}\eta + \vec{D}_u \\ \delta^{(t)}_{LAX}\mathbf{v} &= -\mathbf{u}\delta^{(x)}\mathbf{v} - \mathbf{v}\delta^{(y)}\mathbf{v} - g\delta^{(y)}\eta + \vec{D}_v. \end{aligned} \tag{5a}$$

Equations of continuity:

$$\begin{aligned} \delta^{(t)}_{LAX}\eta = &-[h+\eta](\delta^{(x,t+1)}\mathbf{u} + \delta^{(y,t+1)}\mathbf{v}) \\ &- \mathbf{u}\delta^{(x)}[h+\eta] - \mathbf{v}\delta^{(y)}[h+\eta], \end{aligned} \tag{5b}$$

$\vec{D}_u$ and $\vec{D}_v$ are either $\vec{D}_{u,v} = 0$ or correspond to eq. (4).

Each parameter at point $P(x, y, t + \Delta t)$ depends on the adjacent points $P(x + \Delta x, y, t)$, $P(x - \Delta x, y, t)$, $P(x, y + \Delta y, t)$, $P(x, y - \Delta y, t)$ (explicit numerical integration scheme) and the *Lax*-operator is determined for the point $P(x, y, t)$ at the previous time level. The condition of stability of the numerical scheme (eq. 5) is the Courant-Friedrich-Levy (CFL) criterion: $\frac{\Delta x + \Delta y}{\Delta t} < c$. The velocity c represents the travel velocity of the tsunami wave with $c = \sqrt{g[h + \eta_{\max,t}]}$, and $\Delta t, \Delta x, \Delta y$ are the time and spatial increments, respectively. The subscripts *max* and *t* represent the maximum wave elevation in the computational domain at time *t*. Hence, the time step, being derived by the CFL criterion, varies with time. A further improvement is the application of the *Lax*-operator to each parameter at point $P(x, y, t)$ to increase the stability of the numerical scheme. The implementation of the *LAX*-operator allows the model to run without an additional diffusion term like μ $(\nabla^2\eta)$ (see e.g. Marchuk & Anisimov 2001), where μ represents the kinematic viscosity.

The computational domain of the entire model generally consists of a generation (impact model) and the propagation domain and run-up zone. The impact simulations provide the initial conditions for the wave propagation model (Boussinesq approach) given by eqs (1)–(4). To simulate the propagation in the near-shore area and run-up, the MOST code is used, which is described in greater detail in the next section. To simulate open ocean boundaries conditions (avoiding reflections), a layer of 200 extended cells is added to each side of the wave propagation domain. The extension zone is implemented by a layer of cells with increasing cell-size according to: $dx^{\text{extcell}}_{i+1} = a \cdot dx^{\text{extcell}}_{i}$ where a is between 1.01 and 1.03. If $a \gg 1.03$ reflections occur at cell boundaries. A similar method is utilized in the iSALE code to prevent reflections of waves at the grid boundaries (see Section 2.3).

For the model results in the present study, we used the Boussinesq equation because dispersion is the crucial process during the propagation of the waves. The result of dispersion will be shown as a decaying wave amplitude with distance r to the point of impact proportional to r^{-1} in Section 4.

3.2 Run-up

The calculation of the tsunami wave run-up is a complex problem; a variety of methods have been proposed (Synolakis 1987; Harbitz & Pedersen 1992; Marchuk & Anisimov 2001; Titov & Synolakis 1995, 1998). Among them, different assumptions for the solution of this problem can be distinguished. Analytical approaches often emanate from linear or, at least, piecewise linear geometries in the coastal areas (Kanoglu & Synolakis 1998). The accuracy of numerical or semi-numerical (Harbitz & Pedersen 1992) methods is strongly affected by the spatial resolution.

To compute the run-up, the MOST (method of splitting tsunamis) code is used, developed by Titov & Synolakis (1995, 1998). MOST uses SWE to consider the propagation of waves along the shoreline. The MOST code is made up of two arrays: A, B. In the array A the wave propagation is computed by the SWE Array B is nested into array A and covers the region where the method of the moving boundary is used in order to compute the runup of the waves (see Fig. 4). Fig. 4 defines in a simple sketch the computational parameters along the shoreline. The basic assumption is a straight line between the last 'wet point' (n and $n - 1$ in Fig. 4) and the position of the shoreline. New computational points are added according to the flow velocity over land. Within MOST, the characteristics of tsunami waves are always discretized by a constant number of grid points. During shoaling and run-up, the wavelength decreases as MOST reduces the spatial step size to keep a constant number of characteristic grid points along the wave. A more comprehensive

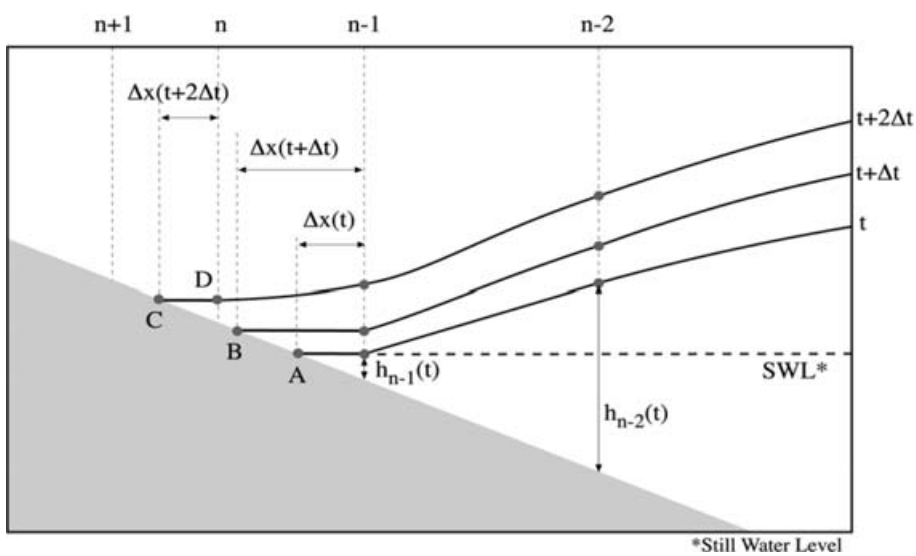

Figure 4. Schematic sketch of the computation of the run-up process along the shoreline using the MOST code (after Titov & Synolakis 1995).

description about run-up algorithm may be drawn from Titov & Synolakis (1995).

The algorithm to compute the run-up used in MOST is very similar to a method proposed by Marchuk & Anisimov (2001). This method considers only a '1+1' propagation and run-up problem (Marchuk & Anisimov 2001), an extension to a '2+1' problem to compute the propagation and run-up with only one model is in progress.

However, the MOST is much more reliable at present state. It is tested against laboratory experiments and analytically solvable problems (Titov & Synolakis 1995, 1998). These studies show that MOST reproduces reliable run-up values also for breaking tsunami waves; even if a highly non-linear 2-D wave-breaking algorithm, for example, given in Chen *et al.* (2000), is not implemented. Additionally, it has been shown that MOST is capable to simulate the run-up of real tsunami events, for example, the 1994 Kurils Islands

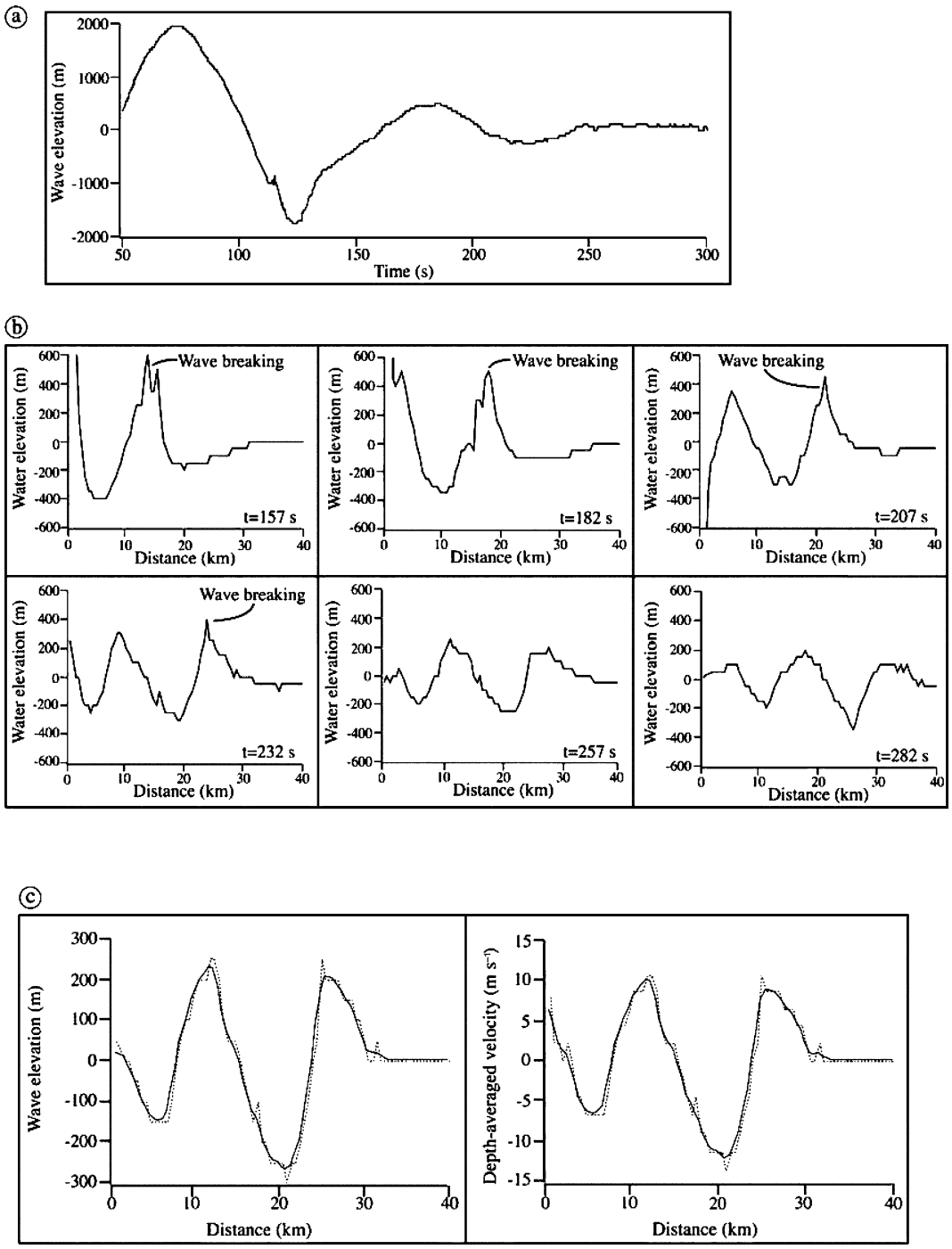

Figure 5. (a) Recorded wave elevation versus time using iSALE beginning 50 s after impact. (b) position of the water surface in the spatial resolution of the wave propagation model after 157, 182, 207, 232, 257 and 282 s. (c) Initial conditions for the wave propagation. The dotted lines represent the original data (see Fig. b) and the solid lines are smoothed.

© 2006 The Authors, *GJI*, **167,** 77–88
Journal compilation © 2006 RAS

Tsunami (Titov & Synolakis 1998), the 1996 Peru Tsunami (Titov & Synolakis 1998), the 1993 Okushiri Tsunami (Titov & Synolakis 1998) and the 1998 Papua New Guinea Tsunami (Synolakis *et al.* 2002; Okal *et al.* 2002).

3.3 Defining initial conditions

Modelling the evolution of impact induced tsunami waves from (i) generation to (ii) propagation to (iii) the final run-up of the wave on the coast requires different numerical solutions schemes. To deal with the specific condition at each of those evolution stages we have constructed a chain of different models covering different scales in time and space, which are (i) the iSALE code for the impact simulation (Section 2), (ii) the wave propagation model (Section 3.1) and (iii) the MOST code for the run-up (Section 3.2). The models are carried out in exactly this order. Due to the complete different structure of the utilized codes (in particular between iSALE and the wave propagation code), it is of no advantage to connect them directly, but instead to define appropriate boundary/interface conditions to transfer the required information (wave elevation and velocity field) from one model to the following one. This is most crucial for the connection between iSALE and the wave propagation code. There are basically three conditions which must be fulfilled to avoid severe numerical artefacts in the calculations: (a) The shock wave, induced at the early stage of the impact, must be decayed since the wave propagation code can not deal with compressive waves, (b) vertical movements of the water column have to be small because in the wave propagation code it is assumed that vertical velocity components can be neglected (condition for BE) (c) wave breaking is a turbulent phenomena which is not modelled very well in the iSALE code but is certainly beyond the capability of the wave propagation model.

The shock wave (a) does not cause any difficulties since shock waves travel much faster (approximately half as fast as the original impact velocity, which is >10 km s^{-1}) than surface waves and decay very quickly by $\sim r^{-2}$ (Melosh 1989), where r is the distance to the point of impact. Therefore, any interference between shock wave and the tsunami can be neglected after $\sim$8–10 s in 40 km distance. To satisfy the conditions (b) and (c) we have to look at a specific example. The panels in Figs 5(a), (b) and (c) illustrate the time and spatial evolution of the wave characteristic by means of an impact of a 800 m meteorite (in diameter) with a velocity of 10.2 km s^{-1} into a 5000-m-deep ocean (compare with snapshot series in Fig. 3). To meet the condition (b), namely that the vertical velocity component needs to be small to allow the application of the BE in the wave propagation code, the oscillation of the central peak must be damped down. Fig. 5(a) shows a time series of the elevation of the water column at the centre (point of impact). The time on the x-axis starts when the central peak begins to form (after $\sim$50 s) by the water rushing back into the excavated cavity. After 250 s vertical movements can be neglected. In Fig. 5(b) each panel shows a snapshot of the water elevation versus distance from point of impact for a series of subsequent time steps. From these figures it can be deduced that three distinct waves are formed by the collapse of the water cavity and subsequent oscillations of the water column (compare the number of oscillations in Fig. 5a). Very steep waveforms in Fig. 5(b) at $t = 157$–232 s indicate breaking of the waves. In order to satisfy condition (c), namely that no wave breaking occurs, the transition between iSALE and the wave propagation model can not take place before 257 s, as illustrated in Fig. 5(b). In all examples we have calculated so far the wave breaking condition (c) was always the one defining the point in time for the transition between the two codes. We have not investigated thoroughly, whether the temporal order, when each of the conditions (a–c) are fulfilled, stays the same or whether all three conditions (a–c) must be checked for each different impact scenario (varying water depth, impact velocity, impactor size). Certainly condition (a), the shock wave decay, is always satisfied first but there might be scenarios possible, where the oscillations of the central peak do not produce breaking waves.

We also compared the wave pattern between iSALE, running it much longer than shown in Fig. 5(b), with the results from the wave propagation model using the wavefield from Fig. 5(b) at $t = 257$ s. We obtained very similar results so we conclude that numerical artefacts from the transition between the two different codes can be ruled out.

Apart from the wave elevation, the depth-averaged radial velocity field is also required as initial conditions for the wave propagation code. For the given example both data sets are shown in Fig. 5(c). In order to achieve stable numerical solutions the data sets are smoothed with the aid of a binomial algorithm. Deviations in elevation at each point are usually less than the spatial resolution of iSALE. Depth-averaged velocities are generally in good agreement with the equation for the travel velocity of tsunami waves: $u_i = \eta_i \cdot \sqrt{g[h_i + \eta_i]}$, where u_i is the velocity at position i, h_i the water depth, η_i the wave elevation and g represents gravity. Since vertical impacts produce radial wave patterns, the initial wave elevation and the depth-averaged velocity are projected onto a circle with respect to the distance to the point of impact (see Fig. 6). Thus, the initial conditions of the wave propagation model cover the entire area of this circle. The projection of the depth-averaged velocity is realized with respect to the two components of the horizontal velocity field required in the wave propagation model.

The transition between the wave propagation code and MOST is easily done by the input of wave elevation data and the horizontal velocities into MOST at a point of time where the main pattern of the tsunami wave is in the range of the array (A) of the MOST code (see Fig. 4). Surface elevation and the velocity field in this region of the wave propagation model serve as initial conditions of the MOST code.

4 EXAMPLE: AN IMPACT INTO AN OCEANIC ENVIRONMENT AND PROPAGATION OF SUBSEQUENT TSUNAMI WAVES OVER AN ARTIFICIAL BATHYMETRY

To demonstrate the capability of the proposed solution scheme we simulate the tsunami wave generation, propagation and run-up by means of an impact onto an artificial marine environment. In this example, the impactor is 800 m in diameter and hits an ocean with a water depth of 5000 m. The geometry of the basin is given in Fig. 6. The geometry itself is subdivided into two parts: a constant depth part of 5000-m-deep water and a constant slope of 1:25 towards to the shoreline. The parameter C gives the distance between the impact centre and the initial shoreline; thus the distance from the impact centre to the toe of the beach is $C - 250$ km $= 750$ km for $C = 1000$ km. In order to show the wave evolution for different C's, we set C to $C_1 = 1000$ km as given in Fig. 6, $C_2 = 2000$ km, and $C_3 = 3000$ km. The width of the basin is kept constant at $W = 500$ km for the different cases. The wave elevation as a function of time is measured every two kilometres (gauge points) along the section A-A′. Fig. 7(a) gives two of such time series at distances

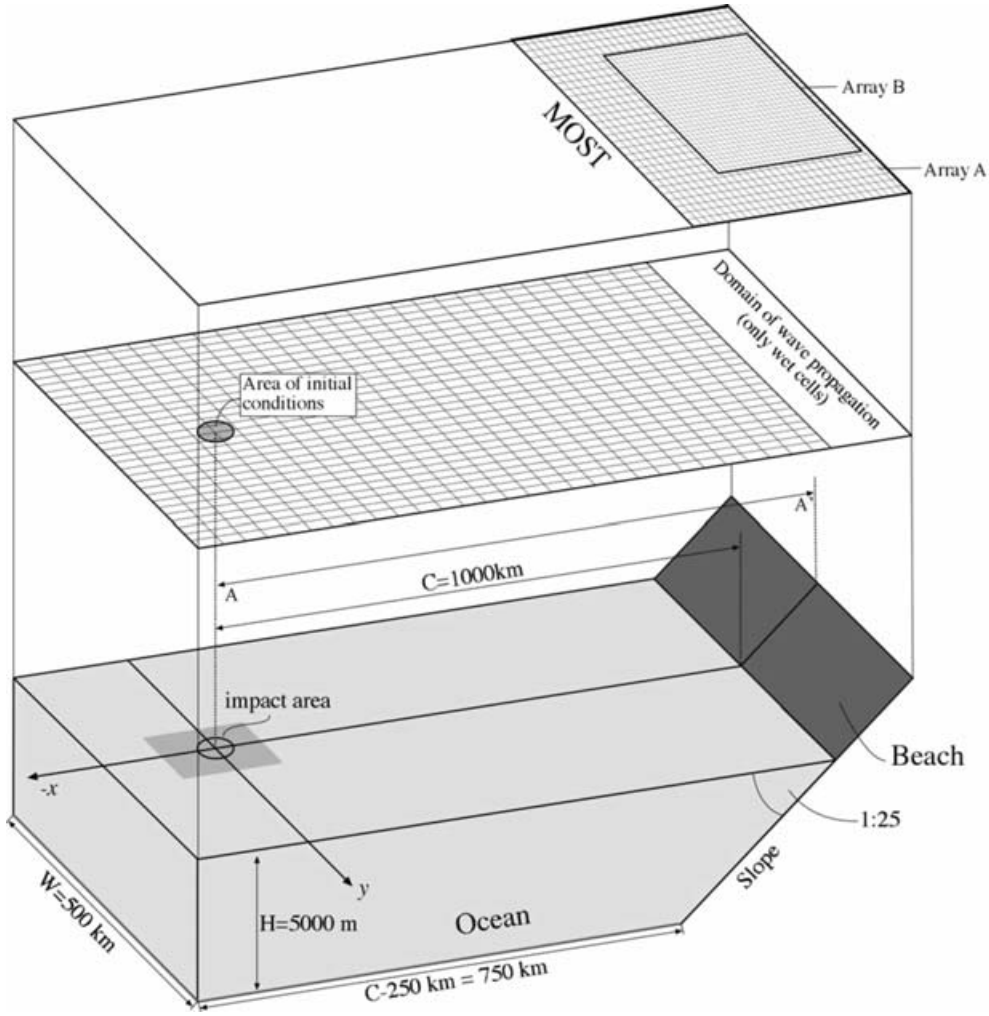

Figure 6. The lower panel gives and example bathymetry with C as the distance between the point of impact and the shoreline. Along the section A-A′, the wave elevation is recorded by gauge points. The impact area is highlighted by the circle. The middle panel illustrates the domain of the wave propagation, covering only the wet part of the example bathymetry. Water deflection due to the impact is implemented as initial conditions according to Fig. 6(c). The two upper panels depict the arrangement of arrays for the wave propagation as well as the arrays A and B used in MOST.

of 100 km (dashed line) and 300 km (solid line) from the impact centre demonstrating that the wave height is significantly lower at 300 km compared to 100 km. Furthermore the period of the wave increased. The time series of the gauge points along the section A-A′ can be used to generate a plot of the maximum wave amplitude as a function of the distance to the impact centre. Fig. 7(b) represents such a diagram which shows that the results are in agreement with dispersive wave theory: the damping of the wave amplitudes (solid lines) are proportional to r^{-1} given by the dashed line. (Fig. 7b). The dotted line in this figure is a wave damping proportional to $r^{-0.5}$ as it would be the case for the non-dispersive theory. However as the pattern of the individual wave evolutions show, the wave amplitudes increase again from a certain distance to shore. This process, being known as shoaling, begins when the waves enter the slope. The right ends of the graphs mark the wave height just before the inundation begins, which is associated to locations close to the shoreline. For the case $C_1 = 1000$ km, the wave height at the beach toe is $A_{bt} =$ 4.61 m and the graphs ends at $A_s = 9.66$ m. For $C_2 = 2000$, A_{bt} is 1.54 m and $A_s = 4.56$ m, for $C_3 = 3000$ km, $A_{bt} = 0.8$ m and $A_s =$ 1.8 m.

The run-up value (run-up) is defined as the vertical distance between the initial position of the shoreline to its position at maximum inundation for each point along the shore. Fig. 7(c) gives the run-up along the coasts for all cases whereas R_1 marks the case $C_1 =$ 1000 km, R_2 is the case $C_2 = 2000$ and R_3 represents the case $C_3 =$ 3000 km. The distribution of the run-up along the coast with consistently higher values in the central part can be ascribed to the linear character of the shoreline and the circular character of the source.

5 SUMMARY AND FUTURE PROSPECTS

In order to model the generation, propagation and run-up of tsunamis caused by oceanic impacts, we use a numerical strategy consisting of impact simulations with the iSALE code and the calculation of the tsunami wave propagation and run-up. The newly developed wave propagation model is based on dispersive (simplified BE) and non-dispersive (SWE) equations. The MOST code is utilized to compute the run-up.

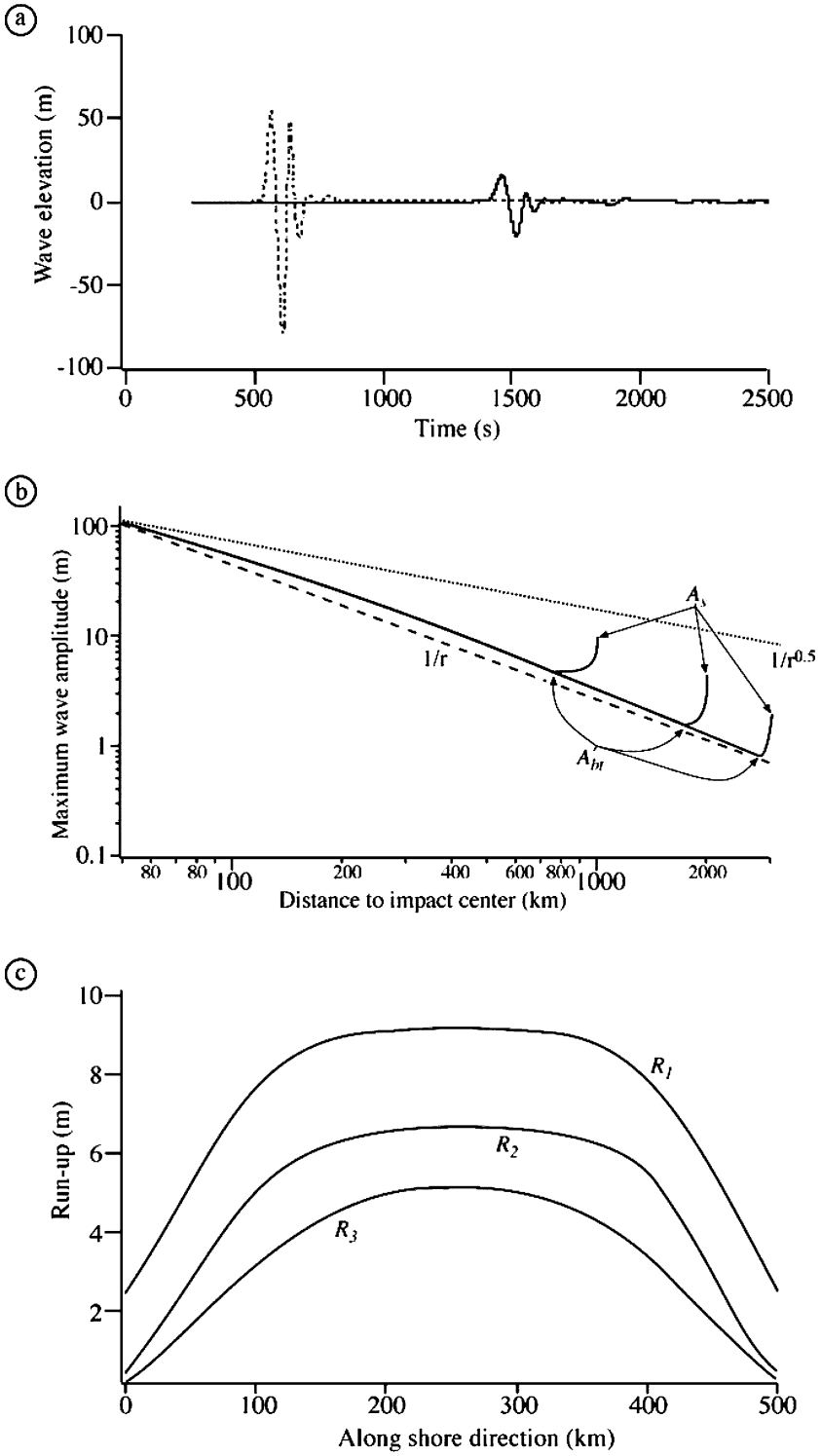

Figure 7. (a) Tide gauge records 100 km (dashed line) and 300 km (solid line) from the impact centre to illustrate the decay of the wave height by dispersion. (b) log–log plot of the maximum wave amplitude versus distance to the impact centre (solid lines). The dotted line shows the damping of the wave elevation obeying a function proportional to $r^{-0.5}$; the dashed line resembles damping proportional to r^{-1}. (c) Run-up height along the shoreline of the different distances to the impact area.

In the present approach, the impact and the tsunami model are not directly connected in one model. The wave pattern is first calculated by the impact model (iSALE) and then the position of the water surface (wave elevation) is used as a boundary condition in the tsunami wave propagation model. By means of a simple example the complexity of propagation and run-up of a tsunami wave is demonstrated although a more sophisticated analysis is required and will be subject of upcoming investigations. However, the presented example indicates, how the amplitude of a tsunami wave is linked to the boundary

conditions, namely the given bathymetry and the impactor-water depth ratio.

The combination of both models allows the computation of a wide range of oceanic impacts, ranging from deep water to shallow water impacts and is only restricted by the maximum computable grid resolution in the impact calculations. For instance very large impactors and very shallow water ($\gamma < \sim 0.2$) cannot be resolved yet. Future work will focus on the method how to determine more impartially the distance where both models are linked. Furthermore a parameter study over a broad range of γ-ratios and artificial and natural bathymetries is in progress.

ACKNOWLEDGMENTS

Our study was supported by the Deutsche Forschungsgemeinschaft (Grant Ba 1011/21-1+2 and WU 355/5-1). Additionally, we thank two anonymous reviewers for their very constructive comments, which improved the quality of the manuscript significantly. We are also very grateful for the support provided by Costas Synolakis and Jose Borerro of the Tsunami Research Center at the University of Southern California, Los Angelos.

REFERENCES

Amsden, A.A., 1973. Numerical calculations of surface waves: a modified ZUNI code with surface particles and partial cells. LA-5146 Report. Los Alamos National Laboratories, Los Alamos, New Mexico.

Amsden, A.A., Ruppel, H.M. & Hirt, C.W., 1980. SALE: a simplified ALE computer program for fluid flows at all speeds, LA-8095 Report. Los Alamos National Laboratories, 101, Los Alamos, New Mexico.

Anderson, C.E. Jr, 1987. An overview of the theory of hydrocodes, *Int. J. Impact Engng,* **5,** 33–59.

Artemieva, N.A. & Shuvalov, V.V., 2002. Shock metamorphism on the ocean floor (numerical simulations), *Deep Sea Res, Part II,* **49,** 959–968.

Beji, S. & Nadaoka, K., 1996. A formal derivation and numerical modelling of the improved boussinesq equationss for varying depth, *Ocean Engineering,* **23,** 691–704.

Chen, Q., Kirby, J.T., Dalrymple, A.R., Kennedy, A.B. & Chawla, A., 2000. Boussinesq modeling of wave transformation, breaking and runup. II: 2D, *Journal of Waterways, Port, Coastal, and Ocean Engineering*. **126/1,** 48–56.

Collins, G.S. & Wünnemann, K., 2005. How big was the Chesapeake Bay impact? Insights from numerical modelling, *Geology*. **33,** 925–928.

Collins, G.S., Melosh, H.J. & Ivanov, B.A., 2004. Modeling damage and deformation in impact simulations, *Meteoritics and Planetary Science,* **39,** 217–231.

Crawford, D.A. & Mader, C.L., 1998. Modeling asteriod impact and tsunami, *Science of Tsunami Hazards,* **16**(1), 21–30.

Gault, D.E. & Sonett, C.P., 1982. Labratory simulation of pelagic asteriodal impact: atmospheric injections, benthic topography, and the surface wave radiation field, *Spec. Pap. Geol. Soc. Am.,* **190,** 69–92.

Gersonde, R. *et al.*, 1997. Geological record and reconstruction of late Pliocene impact of the Eltanin asteroid in the Southern Ocean, *Nature,* **390,** 357–363.

Goldin, T.J., Wünnemann, K., Melosh, H.J. & Collins, G.S., 2005. Hydrocode modelling of the Sierra Madera impact structure, 36th LPSC.

Harbitz, C.B. & Pedersen, G., 1992. Model theory and analytical solutions for large water waves due to landslides. Preprints Series Institut of Mathematics, University of Oslo*,* **4,** 17.

Ivanov, B.A., Deniem, D. & Neukum, G., 1997. Implementation of dynamic strength models into 2D hydrocodes: Application for atmospheric breakup and impact cratering, *International Journal of Impact Engineering,* **17,** 375–383.

Ivanov, B.A. & Artemieva, N.A., 2002. Numerical modeling of the formation of large impact craters, in *Catastrophic Events and Mass Extinctions: Impact and Beyond*, *Geological Society of America, Special Paper,* **356,** 619–630.

Kanoglu, U. & Synolakis, C.E., 1998. Long wave runup on piecewise linear topographies, *Journal of Fluid Mechanics,* **374,** 1–28.

Knowles, C.P. & Brode, H.L., 1977. The theory of cratering phenomena, an overview, in *Impact and Explosion Cratering*, pp. 369–895, eds Roddy, D.J., Pepin, R.O. & Merrill, R.B., Pergamon, New York.

Lynett, P. & Liu, P.L.-F., 2002. A numerical study of submarine landslide generated waves and runup, *Proceedings of the Royal Society London,* **458,** 2285–2910.

Mader, C.L., 1988. *Numerical Modeling of Water Waves*, University of California Press, Berkeley, California.

Mader, C.L., 1998a. Modeling Tsunami inundation of Japan, *Science of Tsunami Hazards,* **16**(1), 11–16.

Mader, C.L., 1998b. Modeling the Eltanian asteriod tsunami, *Science of Tsunami Hazards,* **16/1,** 17–20.

McGlaun, J.M. & Thomspon, S.L., 1990. CTH : A Three-Dimensional Shock Wave Physics Code, *International Journal of Impact Engineering,* **10,** 351–360.

Marchuck, A.G. & Anisimov, A.A., 2001. A method for numerical modeling of tsunami wave run-up on coast of an arbitrary profile, *ITS 2001 Proceedings,* **7,** 933–940.

Matsui, T., Imamura, F., Tajika, E., Nakano, Y. & Fujisawa, Y., 2002. Generation and propagation of a tsunami from the Cretaceous-Tertiary impact event, in *Catastrophic events and mass extinctions: impacts and beyond*, pp. 69–77, eds Koeberl, C. & MacLeod, K.G., Geological Society of America, Boulder, Colorado, Special Paper 356.

Melosh, H.J., 1989. *Impact Cratering: A Geological Process*, Oxford University Press, New York, p. 245.

Okal, E.A., Borrero, J.C. & Synolakis, C.E., 2002. Solving the puzzle of the 1998 Papua New Guinea tsunami: The case for a slump, in *Solutions to Coastal Disasters*, pp. 863–877, eds Wallendorf, L. & Ewing, L., Amer. Soc. Civil Eng.

O'Keefe, J.D. & Ahrens, T.J., 1999. Complex craters: Relationship of stratigraphy and rings to impact conditions, *J. geophys. Res.,* **104,** 27 091–27 104.

Ormö, J., Shuvalov, V.V. & Lindström, M., 2002. Numerical modeling for target water depth estimations of marine target impact craters, *J. geophys. Res.,* **107**(E12), 5120.

Paine, M.P., 1999. Asteriod impacts: The extra hazard due to tsunami, *Science of Tsunami Hazards,* **17**(3), 155–166.

Peregrine, D.H., 1967. Long waves on a beach, *J. Fluid Mech.,* **27,** 815–827.

Press, W.H., Teukolsky, S.A., Vetterling, W.T. & Flannery, B.P., 1992. *Numerical Recipes in C: The Art of Scientific Computing*, 2nd edn, Cambridge University Press, New York, p. 994.

Roddy, D.J., Schuster, S.H., Rosenblatt, M., Grant, L.B., Hassig, P.J. & Kreyenhagen, K.N., 1987. Computer simulation of large asteroid impacts into oceanic and continental sites—preliminary results on atmospheric, cratering and ejecta dynamics, *International Journal of Impact Engineering,* **5,** 525–541.

Shuvalov, V.V., 1999. Multi-dimensional hydrodynamic code SOVA for interfacial flows: applications to the thermal layer effect, *Shock Waves,* **9,** 382–390.

Shuvalov, V.V., Dypvik, H. & Tsikalas, F., 2002. Numerical simulations of the Mjolnir marine impact crater, *J. Geophys. Res.,* **107,** 10.1029/2001JE001698.

Synolakis, C.E., 1986. The runup of long waves, Ph.D. Thesis, California Institute of Technology, Pasadena, California, 228.

Synolakis, C.E., 1987. The Runup of Solitary Waves, *J. Fluid Mech.,* **185,** 523–545.

Synolakis, C.E., Bardet, J.P., Borrero, J., Davies, H., Okal, E., Silver, E., Sweet, J. & Tappin, D., 2002. Slump origin of the 1998 Papua New Guinea tsunami, *Proceedings of the Royal Society of London, Ser. A,* **458,** 763–789.

Tadepalli, S. & Synolakis, C., 1994. The runup of N-Waves on sloping beaches, *Proc. Royal Society London,* **A445,** 99–112.

Thompson, S.L. & Lauson, H.S., 1972. Improvements in the Chart D radiation-hydrodynamic CODE III: Revised analytic equation of state. Rep. SC-RR-71 0714, Sandia Natl. Lab, Albuquerque, N.M., 119.

Titov, V.V. & Synolakis, C.E., 1995. Modeling of breaking and nonbreaking long–wave evolution and runup using VTCS-2, *Journal of Waterways, Ports, and Ocean Engineers,* **121,** 308–316.

Titov, V.V. & Gonzalez, F.I., 1997. Implementation and testing of the method of splitting tsunamis (MOST), NOAA Technical Memorandum, ERL PMEL112.

Titov, V.V. & Synolakis, C.E., 1998. Numerical modeling of tidal wave runup, *Journal of Waterways, Ports, and Ocean Engineers,* **124,** 157–171.

Ward, S.N. & Asphaug, E., 2000. Asteroid impact tsunamis: a probabilistic hazard assessment, *Icarus,* **145,** 64–78.

Weiß, R., Wünnemann, K. & Bahlburg, H., 2003. Oceanic impacts, tsunamis, and the influence of the water depth on the quantitiy and characteristics of the generated waves. Third International Conference on Large Meteorite Impact 5.-7. August, Nördlingen, Nummer 4081.

Wünnemann, K. & Lange, M.A., 2002. Numerical modeling of impact-induced modifications of the deep-sea floor, *Deep-Sea Research II,* **49,** 669–981.

Wünnemann, K. & Ivanov, B.A., 2003. Numerical modelling of impact crater depth-diameter dependence in an acoustically fluidised target, *Planetary and Space Science,* **51,** 831–845.

Wünnemann, K., Morgan, J.V. & Jödicke, H., 2005. Is Ries crater typical for its size? An analysis based upon old and new geophysical data and numerical modelling, in eds Kenkman, K., Hörz, F. & Deutsch, A., Large meteorite impacts III, Geological Society of America Special Paper 384, 67–83.

Wünnemann, K., Collins, G.S. & Melosh, H.J., 2006. A strain-based porosity model for use in hydrocode simulations of impats and implications for the transient-crater growth in porous targets, *Icarus,* **180,** 514–527.